ELECTROCHEMISTRY

Amorphization mechanism of $SrIrO_3$ electrocatalyst: How oxygen redox initiates ionic diffusion and structural reorganization

Gang Wan[1], John W. Freeland[2], Jan Kloppenburg[3], Guido Petretto[3], Jocienne N. Nelson[4], Ding-Yuan Kuo[5], Cheng-Jun Sun[2], Jianguo Wen[6], J. Trey Diulus[7], Gregory S. Herman[7], Yongqi Dong[1,2,8], Ronghui Kou[2], Jingying Sun[9], Shuo Chen[9], Kyle M. Shen[4,10], Darrell G. Schlom[5,10,11], Gian-Marco Rignanese[3], Geoffroy Hautier[3], Dillon D. Fong[1]*, Zhenxing Feng[7]*, Hua Zhou[2]*, Jin Suntivich[5,10]*

The use of renewable electricity to prepare materials and fuels from abundant molecules offers a tantalizing opportunity to address concerns over energy and materials sustainability. The oxygen evolution reaction (OER) is integral to nearly all material and fuel electrosyntheses. However, very little is known about the structural evolution of the OER electrocatalyst, especially the amorphous layer that forms from the crystalline structure. Here, we investigate the interfacial transformation of the $SrIrO_3$ OER electrocatalyst. The $SrIrO_3$ amorphization is initiated by the lattice oxygen redox, a step that allows Sr^{2+} to diffuse and O^{2-} to reorganize the $SrIrO_3$ structure. This activation turns $SrIrO_3$ into a highly disordered Ir octahedral network with Ir square-planar motif. The final Sr_yIrO_x exhibits a greater degree of disorder than IrO_x made from other processing methods. Our results demonstrate that the structural reorganization facilitated by coupled ionic diffusions is essential to the disordered structure of the $SrIrO_3$ electrocatalyst.

INTRODUCTION

The production of materials and fuels from widely available molecules is one of the most important challenges facing 21st-century society (*1*–*3*). Electrocatalysts function by providing environments conducive to the fuel and material electrosynthesis (*4*, *5*). However, developing high-performance electrocatalysts is far from straightforward. One of the major hurdles is the lack of information regarding the evolving structure of the electrocatalysts during the electrochemical operations. This knowledge gap is particularly problematic for the oxygen evolution reaction (OER), where the reaction environment is highly oxidizing and can rearrange the structure of the electrocatalyst (*6*–*8*). Given that the OER, the key electro-oxidation reaction, is one of the major causes of inefficiency in the fuel and material electrosynthesis (*1*, *2*), understanding the structural and chemical evolution of the electrocatalyst during the OER is essential to the development of active future electrocatalyst materials and, more broadly, to the prospect of materials and energy sustainability.

The search for more active and stable OER electrocatalysts has motivated several investigations into the structure-activity relationships of perovskite-based oxides (*9*, *10*). Aside from studying how surfaces stabilize adsorbates, a number of theoretical and experimental studies have indicated that high-performance electrocatalysts can undergo interfacial transformations during the OER, in particular, from the crystalline to amorphous structure (*11*–*14*). For instance, $Ba_{0.5}Sr_{0.5}Co_{0.8}Fe_{0.2}O_{3-\delta}$ (BSCF) particles have been reported to undergo surface morphology and local structure change during the OER in alkaline media. This transformation is accompanied by metal dissolution and increased capacitive and OER current (*7*, *8*, *15*). Similar phenomena have been observed for active Ir-based complex oxides (*16*, *17*), a finding that had led to a suggested relationship between structural transformation and OER (*6*, *18*–*20*). The current picture is that the transformation process involves the collapse of the pristine structure and the reformation of Ir compounds, for example, segregated Ir oxides/hydroxides (*16*, *21*) associated with higher degrees of disorder (*6*). This amorphization could originate from a direct metal dissolution or electrochemically from the close proximity of the O p-band to the Fermi level (*16*, *22*). In the latter mechanism, the lattice oxygen redox can be activated, leading to the lattice oxygen activation, a process that allows the lattice oxygen to directly participate in the electrochemical reaction. This participation of lattice oxygen in the OER has also been suggested to be a source of surface restructuring in BSCF, which has caused a cycle of dissolution/deposition during the OER (*7*). However, there remain many critical questions, for example, how the lattice oxygen activation is connected to metal dissolution, and whether lattice oxygen activation occurs simultaneously or sequentially with metal dissolution. It is unclear how the lattice oxygen activation leads to surface transformation and why the resulting amorphous structure is distinct from other amorphous oxides made electrochemically or thermally.

In this work, we provide atomic-level insight into the crystalline-to-amorphous transformation and describe a mechanism that holistically

[1]Materials Science Division, Argonne National Laboratory, Lemont, IL 60439, USA. [2]X-ray Science Division, Advanced Photon Source, Argonne National Laboratory, Lemont, IL 60439, USA. [3]Institute of Condensed Matter and Nanosciences, Université Catholique de Louvain, Chemin des Étoiles 8, B-1348 Louvain-la-Neuve, Belgium. [4]Laboratory of Atomic and Solid State Physics, Department of Physics, Cornell University, Ithaca, NY 14853, USA. [5]Department of Materials Science and Engineering, Cornell University, Ithaca, NY 14853, USA. [6]Center for Nanoscale Materials, Argonne National Laboratory, Lemont, IL 60439, USA. [7]School of Chemical, Biological, and Environmental Engineering, Oregon State University, Corvallis, OR 97331, USA. [8]National Synchrotron Radiation Laboratory, University of Science and Technology of China, Hefei, Anhui 230026, China. [9]Department of Physics and the Texas Center for Superconductivity, University of Houston, Houston, TX 77204, USA. [10]Kavli Institute at Cornell for Nanoscale Science, Cornell University, Ithaca, NY 14853, USA. [11]Leibniz-Institut für Kristallzüchtung, Max-Born-Str. 2, 12489 Berlin, Germany.
*Corresponding author. Email: fong@anl.gov (D.D.F.); zhenxing.feng@oregonstate.edu (Z.F.); hzhou@aps.anl.gov (H.Z.); jsuntivich@cornell.edu (J. Suntivich)

connects the lattice oxygen activation, metal dissolution, and amorphization in $SrIrO_3$. We focus on $SrIrO_3$, the state-of-the-art OER electrocatalyst in acid (*21*), to understand the origin of its high activity and track its interfacial evolution during the OER, providing the knowledge essential to the future electrocatalyst development. Our experiment begins with an atomically smooth, single-crystalline film of $SrIrO_3$ grown by molecular beam epitaxy (MBE). The use of an epitaxial film allows us to track the structural evolution without concerns over sample heterogeneity such as surface terminations, structural defects, and phases (*23*, *24*). In conjunction with theoretical modeling, we use a suite of synchrotron-based surface-sensitive x-ray techniques and electron microscopy to understand the surface transformation process: surface x-ray diffraction (XRD) and x-ray reflectivity (XRR) to track the crystalline-to-amorphous transformation at the oxide surface and grazing incidence x-ray absorption near-edge spectroscopy (XANES), extended x-ray absorption fine structure (EXAFS), and soft x-ray absorption spectroscopy (XAS) to identify the local geometry/coordination and electronic structure in the amorphous and crystalline layers of $SrIrO_3$.

Our results show that the OER leads to the formation of an active ~2.4-nm-thick amorphous Sr_yIrO_x film atop crystalline, highly defective "$SrIrO_3$." This amorphous structure results from the lattice oxygen activation, which initiates coupled Sr^{2+} and O^{2-} diffusion at the oxide-electrolyte interface. The amorphous Sr_yIrO_x layer protects the underlying $SrIrO_3$ from further amorphization but is ionically conductive, i.e., supports the passage of Sr^{2+} and O^{2-} ions. These ionic movements cause both the amorphous and crystalline layers to undergo additional transformations even after the amorphous Sr_yIrO_x layer has reached a steady-state thickness. We probe the structural and chemical evolution and the atomic details of the active amorphous material, which we find to be a highly disordered, amorphous structure of $Ir^{4+}O_6$ octahedra with Sr^{2+}-Ir^{3+} residue.

RESULTS

Formation of the amorphous layer

An $SrIrO_3$ film was grown on a $DyScO_3$ (110) orthorhombic substrate along the $(001)_{pc}$ orientation (subscript pc denotes a pseudocubic orientation) (*25*). The well-defined oscillations in both XRR and XRD (Fig. 1) indicate a high-quality film-substrate interface and that $SrIrO_3$ is atomically smooth with a starting thickness of 16.0 ± 0.1 nm. To monitor the evolution of the thickness upon OER cycling, we take advantage of the differential sensitivities of XRR and XRD. Specifically, XRR is sensitive to the total film thickness (both crystalline and amorphous layers), while XRD is only sensitive to the crystalline part. After 0.25 hours of cyclic voltammetry (CV) between 1.05 and 1.75 V versus reversible hydrogen electrode (RHE) in 0.1 M $HClO_4$, negligible change to the overall film thickness was observed (15.8 ± 0.4 nm). In this same period, the thickness of the crystalline $SrIrO_3$ decreased from 16.0 ± 0.1 to 13.5 ± 0.5 nm. The difference between the overall film thickness and the thickness due to crystalline $SrIrO_3$ is a result of the growth of a ~2.3 ± 0.3 nm amorphous layer (Fig. 1). From 0.25 to 4 hours, the thickness of the amorphous layer changes minimally, from 2.3 ± 0.3 to 2.4 ± 0.4 nm (Fig. 1), and remains unchanged afterward up to 20 hours of cycling (table S1 and fig. S2). Cross-sectional transmission electron microscopy (TEM) observations confirmed the thickness of the crystalline $SrIrO_3$ layer at ~13.4 nm and the growth and evolution of a 2.4-nm amorphous layer (Fig. 1).

Despite the amorphous layer appearing to reach a steady-state thickness at 0.25 hours, we observe a continual increase in the CV current upon cycling for up to 4 hours (fig. S1). After this point, the current stayed approximately at the same value. While this electrochemical behavior is consistent with what has been reported (*21*), it is interesting that the OER current continued to increase after the amorphous layer has stopped growing, indicating that the amorphous oxide went through additional reorganization after it has finished growing. We will later discuss the mechanism behind this reorganization. First, we show that the OER is necessary to start amorphization. When cycled between 0.8 and 1.0 V versus RHE, which is below the potential required for the OER, both XRR and XRD show that the $SrIrO_3$ film showed no amorphous layer in this pre-OER potential window (Fig. 1). This finding suggests that the transformation from crystalline $SrIrO_3$ to amorphous iridate is driven by the oxidative potential in the range of the OER. This observation is consistent with the recent suggestion that the amorphization is connected to the OER (*6*, *7*, *16*).

Local structure and compositions of the amorphous layer

We probed the structural evolution of the amorphous layer during the first 4 hours of potential cycling using XANES and EXAFS. While care has been made to minimize the time between electrochemistry and x-ray experiments, air exposure could affect surface chemistry. We have, therefore, restricted our analysis to the amorphous layer, which spanned the first nanometers, instead of the topmost surface. To minimize the sample variability, we tracked the progression of the same $SrIrO_3$ sample, starting with Sr L_3-edge. To distinguish the Sr signals from the amorphous layer and the overall film, we performed Sr L_3-edge XANES in both the total electron yield (TEY; which has a probing depth of few nanometers, which is about the thickness of the amorphous layer) and total fluorescence yield (TFY; which has a probing depth that exceeds the total film thickness) modes. We compare the XANES intensities to assess the evolution of the Sr concentration. The Sr L_3-edge XANES reveals that the Sr content decreased in both the amorphous and crystalline layers (Fig. 2) with respect to the initial Sr composition, with the loss being more pronounced in the amorphous layer. After 0.25, 1, and 4 hours, the amorphous layer loses ~27% ("$Sr_{0.73}IrO_x$"), ~65% ("$Sr_{0.35}IrO_x$"), and ~80% ("$Sr_{0.2}IrO_x$") of Sr, while the overall film loses ~0%, ~20%, and ~45% over the same time span. With x-ray photoelectron spectroscopy (XPS), we verified that ~20% of Sr remained in the surface layer after 4 hours (table S2). We note that a previous study of $SrIrO_3/SrTiO_3$ showed that ~20% of Sr remained in the surface layer after 24 hours (*21*), suggesting that ~20% is likely the steady-state Sr concentration.

The observed Sr loss is not surprising given the strong thermodynamic driving force for the Sr dissolution in $SrIrO_3$ (section S7.1). However, it is not understood how the catalyst achieves charge neutrality upon dissolution, i.e., whether the charge compensation occurs via the change in the Ir formal oxidation state or the loss of lattice oxygen. To address this question, we tracked the evolution of the Ir formal oxidation state and local coordination via XANES and EXAFS measurements at the Ir L_{III}-edge. The grazing incidence configuration (GI-XANES and GI-EXAFS) was used to limit the probing depth (~2.2 nm) to the surface amorphous layer (~2.4 to 2.6 nm thick). The Ir L_{III}-edge (Fig. 3) shows a decrease in the white-line intensity at 0.25 hours, indicating that the near-surface Ir formal oxidation state decreases after 0.25 hours. From reference Ir

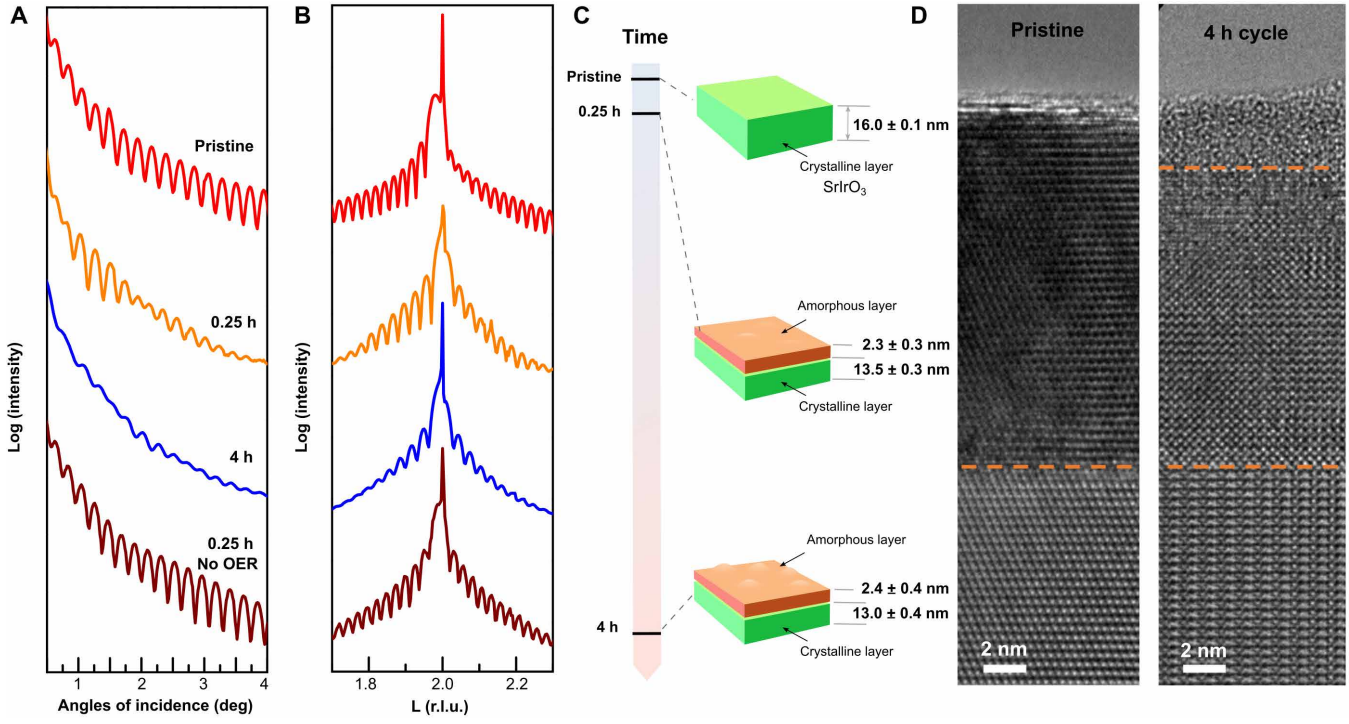

Fig. 1. Growth kinetics of the amorphous IrO_x layer on an $SrIrO_3$ $(001)_{pc}$ film undergoing OER. (**A**) XRR and (**B**) crystal truncation rod of the $SrIrO_3$ film in the pristine state (red) after 0.25 (orange) and 4 hours (blue) of potential cycling between 1.05 and 1.75 V versus RHE and after 0.25 hours (brown) of potential cycling between 0.8 and 1 V versus RHE. r.l.u., reciprocal lattice unit. (**C**) Visual summary of the x-ray thicknesses analyzed from the results shown in (A) and (B). The formed amorphous IrO_x layer appears to reach a steady-state thickness by 0.25 hours. (**D**) Cross-section transmission electron microscopy (TEM) images of the pristine $SrIrO_3$ film after 4 hours of potential cycling between 1.05 and 1.75 V versus RHE. The zone axis of the pristine and cycled $SrIrO_3$ layer is along the $[212]_{or}$ and $[101]_{or}$ directions, respectively (directions were used on the basis of the damage-free TEM sample preparation; see the "Transmission electron microscopy" section in Materials and Methods).

compound measurements, we estimate the Ir formal oxidation state to be 3.1 (± 0.1) at 0.25 hours (fig. S4) and the Ir-O coordination number to be 4.5 (Fig. 3).

The drop in the Ir-O coordination to 4.5 (±0.4) from 6 (±0.6) in pristine $SrIrO_3$ at 0.25 hours implies the loss of the lattice oxygen. This finding is consistent with the observed reduction of the Ir formal oxidation state and Sr stoichiometry. Together, our result suggests that the lattice oxygen left the amorphous layer in a greater quantity than Sr. We note that this conclusion was derived from the transient averages in the Ir oxidation state and Sr composition. While we cannot rule out the possible heterogeneity issue within the amorphous layer, the observed drop in the Ir-O coordination and Sr composition is consistent with the idea that the loss of lattice oxygen plays an essential role in the early stage of the $SrIrO_3$ amorphization. We present the exact values in each transformation stage with error bars. We use these results to assign the nominal composition of the amorphous layer at 0.25 hours as "$Sr_{0.73}Ir^{3.1+}O_{2.28}$." Density functional theory (DFT) calculations show that Sr has higher migration (3.1 eV) barrier than O (1.9 eV) in $SrIrO_3$, suggesting that Sr loss is kinetically inhibited compared to O loss (see fig. S11 and section S7.1 for calculation details).

We propose the mechanism underlying the $SrIrO_3$ transformation based on these observations. First, the high oxidation potential activates the lattice oxygen ($O_{lattice}$), leading to the lattice oxygen loss and the creation of oxygen vacancy (V_{oxygen}). This increase in the oxygen vacancy concentration consequently affects the oxygen diffusion coefficient. The connection between the oxygen vacancy formation and lattice oxygen activation has been discussed (*7*, *11*, *16*). During the lattice oxygen activation ($O_{lattice} + H_2O \rightarrow O_2 + 2H^+ + 2e^- + V_{oxygen}$), the buildup of excess electronic charge reduces the Ir oxidation state, in agreement with the Ir L_{III}-edge XANES. After the lattice oxygen activation step, the lattice oxygen regeneration (i.e., filling of the vacancies, $V_{oxygen} + H_2O \rightarrow O_{lattice} + 2H^+ + 2e^-$) is kinetically sluggish, e.g., slower than the lattice oxygen activation process. In this scenario, oxygen vacancies accumulate to the point where crystalline $SrIrO_3$ experiences structural instability and collapses into Sr-doped amorphous IrO_x. Note that the accumulation of the oxygen vacancy can also enable Sr to migrate. Our DFT calculations demonstrate that removing one or two of the oxygen atoms along its migration pathway can decrease the activation energy of Sr migration from 3.1 to 2.7 and 2.25 eV (see fig. S11 and section S7.1). The beneficial effect of the oxygen vacancy on the Sr migration provides a channel for Sr to migrate away from the crystalline subsurface $SrIrO_3$ layer during electrochemistry. The underlying $SrIrO_3$ layer maintains its crystallinity even after ~40% Sr is lost (according to the TFY Sr L_{III}-edge measurement at 4 hours; Fig. 2). This finding suggests that the Sr loss alone cannot cause amorphization. We thus postulate that it is the coupled O-Sr out-diffusion that caused the amorphization of $SrIrO_3$. Geiger *et al.* (*6*) and Grimaud *et al.* (*16*) have suggested that the Ir formal oxidation state may decrease as the oxygen vacancies form. Our work supports their views and further shows that the metal (Sr) dissolution and the

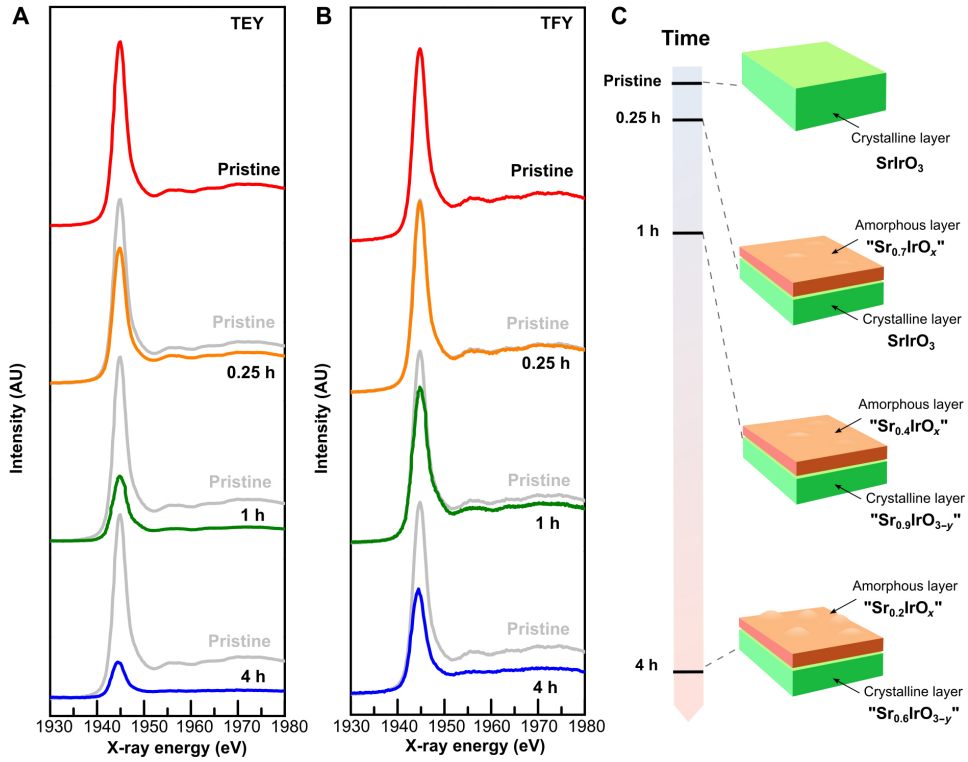

Fig. 2. Sr content in an $SrIrO_3$ $(001)_{pc}$ film undergoing the OER. Sr L_3-edge XANES in the (**A**) total electron yield (TEY; penetration depth ~2 nm) and (**B**) total fluorescence yield (TFY; penetration depth exceeding the total film thickness) configuration. Both TEY and TFY measurements show that Sr continually decreases during the OER cycling. AU, arbitrary units. (**C**) Visual summary with the Sr concentration information as extracted from the Sr L_3-edge XANES, showing a leaching of Sr from the amorphous IrO_x layer even after the amorphization process has stopped.

process of amorphization are coupled through the lattice oxygen activation and that one cannot happen without the other.

Subsequent diffusional reorganization

Having identified how the crystalline-to-amorphous transformation starts at 0.25 hours, we next examine the subsequent reorganization at 1 and 4 hours using Ir L_{III}-edge GI-XANES and GI-EXAFS. The Ir oxidation state and coordination number increase from 3.1 (±0.1) and 4.5 (±0.4) (0.25 hours), respectively, to 3.6 (±0.1) and 5.3 (±0.7) (1 hour), and then to ~3.7 (±0.1) and 5.8 (±0.6) (4 hours) (Fig. 3). Because the Sr composition also decreases during this period, we propose that the Ir oxidation state increases after 0.25 hours to offset the Sr loss and maintain charge neutrality, effectively oxidizing Ir^{3+} to Ir^{4+}. Simultaneously, the oxide regains the lattice oxygen (via the oxygen vacancy filling), gradually restoring the Ir-O coordination. The dynamic behaviors on the oxidation states of surface Ir are confirmed by the Ir M_{III}-edge near-edge XAFS (NEXAFS) detected in TEY mode (fig. S5). During this period, the amorphous oxide also becomes more active for the OER.

We summarize our observations thus far with the following mechanism. The transformation starts with the lattice oxygen activation at high oxidation potential. This lattice oxygen activation leads to the lattice oxygen loss and increased oxygen vacancy concentration. The newly formed oxygen vacancies facilitate the oxygen diffusion and transform the surface $SrIrO_3$ layer into an amorphous Ir^{3+} oxide. At 0.25 hours, the Ir-O coordination number is 4.5 (±0.4), which suggests that the local structure of the amorphous layer at the early stage could have a square-planar structure that is derived from the apical oxygen removal and is stabilized by Sr^{2+}. To assess the energetics of the square-planar geometry, we calculated the energy of the $Sr_{0.5}IrO_2$ structure created by removing O and Sr from perovskite $SrIrO_3$ as a model for Sr-/O-deficient $SrIrO_3$. Our DFT calculations reveal a strong preference for Ir^{3+} to be in a square-planar environment when both Sr and O are removed (fig. S12). This calculation also shows that the Sr diffusion is faster in the presence of the oxygen vacancy, supporting our hypothesis of an open square-planar network that facilitates the Sr loss. We propose that this open square-planar structure facilitates the Sr^{2+} diffusion out of the film. This leads to a strong leaching of Sr^{2+} at 1 and 4 hours. This Sr loss destabilizes the defect-rich structure and causes Ir to reoxidize and form a mixture of Ir^{3+}/Ir^{4+} octahedral clusters (Fig. 4). The final structure is thus a disordered mixture of Ir^{3+}/Ir^{4+} octahedra, which is the result of the coupled diffusion between the anions (O) and cations (Sr) during the amorphization.

Signature of the active moiety

We now discuss what makes the amorphous, disordered iridate structure obtained from $SrIrO_3$ different from the chemically and thermally grown amorphous iridates. We performed NEXAFS at the O K-edge in the TEY mode (with a probing depth of few nanometers) to probe the local Ir-O bonding properties in the amorphous layer. The pristine $SrIrO_3$ (Fig. 4A) shows two peaks at ~529 and ~532 eV, which we assign to the t_{2g} and e_g parentage states based on the similar assignments in rutile IrO_2 (*26*). After 0.25 hours,

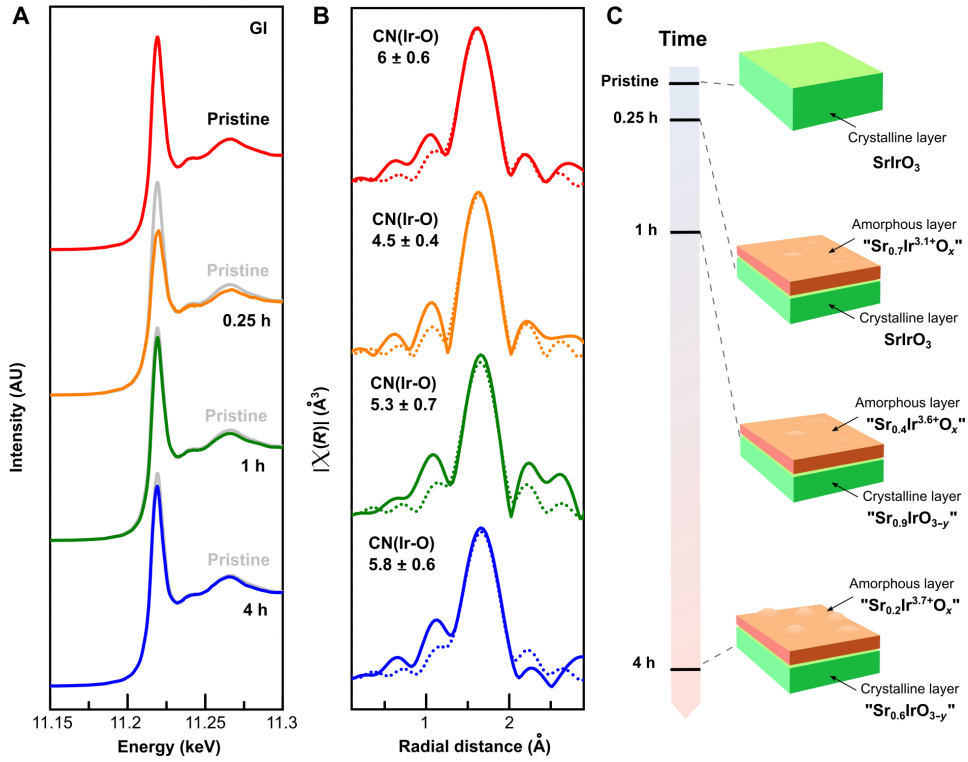

Fig. 3. Electronic structure and local coordination of an $SrIrO_3$ film undergoing the OER. (**A**) Grazing incidence (GI)–XANES and (**B**) GI-EXAFS of Ir L_3-edge show an initial reduction in the Ir formal oxidation state and the coordination number (CN) at 0.25 hours. After 0.25 hours, both the Ir formal oxidation and the coordination number increase back to the initial values before the OER cycling. Both probes have penetration depths of ~5 nm. (**C**) Visual summary of the Ir formal oxidation state extracted from the Ir L_3-edge XANES from the results in (A), showing the evolution of the Ir formal oxidation state during the OER cycling.

the intensity of the t_{2g} peak at ~529 eV drops, while the e_g peak at ~532.5 eV moves to higher energy. The weakening of the first peak intensity is consistent with the decrease in the Ir formal oxidation state, i.e., decreasing amount of empty Ir t_{2g} peak state. The shift in the second peak is attributed to the changing crystal field of the square-planar structure, which changes the energy levels of the O 2p–Ir 5d states (*27*). After 1 hour of cycling, the first peak (nominally t_{2g}) regains intensity. This observation is consistent with the Ir L_{III}-edge result, which shows that the Ir formal oxidation state recovers at the 1-hour point.

After 4 hours, the O K-edge spectrum shows substantially decreased intensity in the low-energy region and a broader peak at higher energy. These observed features are markedly different from those for conventional amorphous IrO_x (*28*, *29*), which exhibits two sharp features corresponding to the nominally t_{2g} and e_g excitations. To understand these changes, we performed a computational survey on all known iridate polymorphs containing Ir^{4+} octahedra with different octahedral connectivities (e.g., anatase, brookite, or rutile; see section S7 and fig. S11). We emphasize that we cannot solve the exact structure of the amorphous layer. Instead, the purpose of this computational analysis is to demonstrate how the local structure of IrO_2 affects the O K-edge by studying a series of model crystalline structures to understand whether the amorphous Sr_yIrO_x structure after long time cycling could be represented by conventional iridate moieties.

DISCUSSION

Our computational results indicate that none of the known iridate polymorphs can replicate the observed, broad O K-edge peak, as all iridate polymorphs exhibit sharp peaks corresponding to the t_{2g} and e_g excitations. Only a highly disordered amorphous model of IrO_2 derived from the reported amorphous TiO_2 structure (*30*) leads to O K-edge spectra, consistent with the experiment (Fig. 4). Thus, we conclude that Sr_yIrO_x is highly disordered. This structural heterogeneity broadens the energy distribution of the t_{2g} and e_g excitations, causing nominally sharp t_{2g} and e_g peaks to blur. The outcome is one broad excitation feature, although the structure contains predominantly the Ir octahedra that should normally exhibit two distinct (t_{2g} and e_g) excitations (figs. S11 and S12). Amorphization leading to the disappearance of the t_{2g} and e_g peaks at the O K-edge has been observed in TiO_2 (*31*). We expect this effect to be even stronger in IrO_2 in view of the smaller crystal field splitting. While we cannot extract the exact iridate structure within the amorphous layer, this observation of the loss of distinctive t_{2g} and e_g excitations in amorphous iridates suggests a high degree of disorder within the amorphous iridate layer atop $SrIrO_3$.

An interesting observation can be made given the energetics regarding different polymorphs. All stable iridate polymorph structures present octahedral environments. Among the five lowest energy structures, we find not only the previously considered brookite and anatase but also the more open hollandite and romanechite structures. The hollandite structure has the lowest energy among the nonrutile polymorphs, indicating that structural reorganizations could favor hollandite-like motifs in the amorphous layer (figs. S13 and S14). The hollandite structure presents open cavities that could accommodate the remaining Sr in the iridate and may explain why Sr diffuses faster after the amorphization. We hypothesize

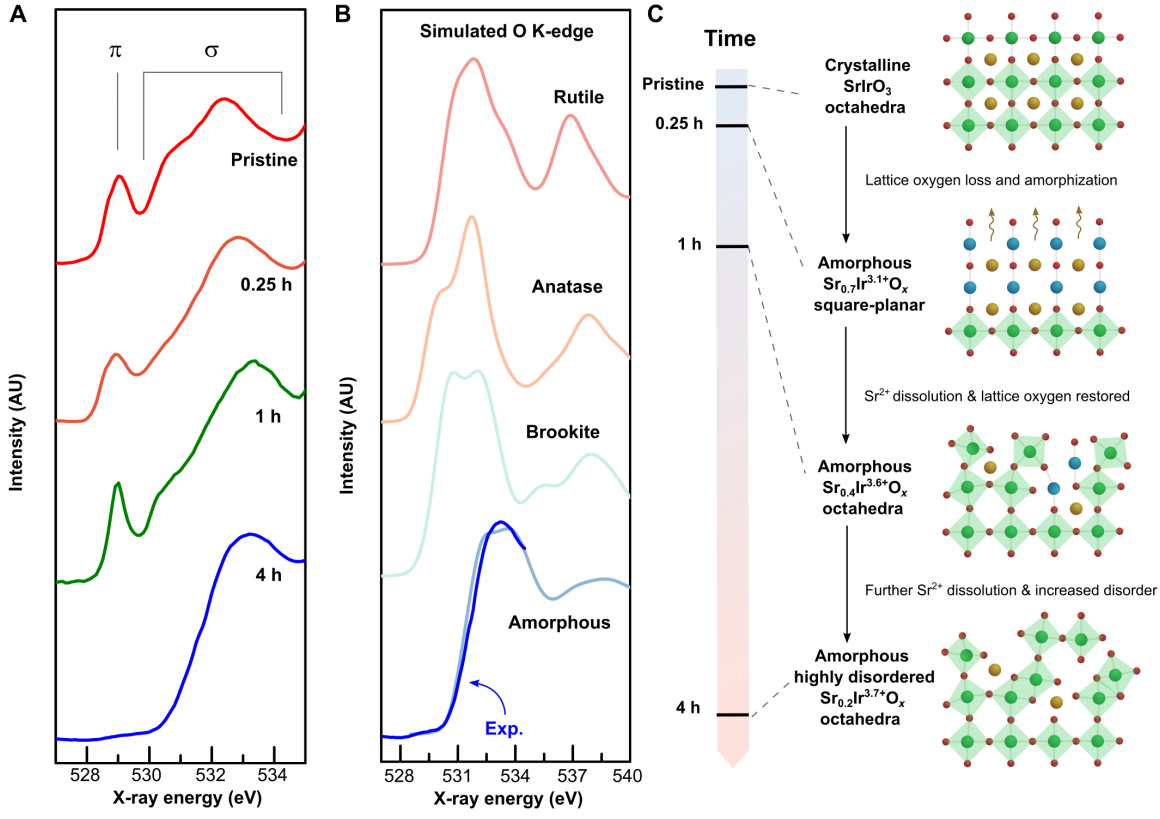

Fig. 4. Local structure of the $SrIrO_3$ film undergoing the OER. Start (**A**) O K-edge NEXAFS of $SrIrO_3$ in TEY mode. The pre-peaks correspond to the O 2p–Ir 5d excitation (π and σ interactions, i.e., the t_{2g} and e_g parentage states). At 0.25 hours, the intensity of the first pre-peak decreases, corresponding to the reduced Ir formal oxidation. At 1 hour, the pre-peak regains the intensity, corresponding to the Ir reoxidation. At 4 hours, the pre-edge features transform into a broad peak. We ascribe this result to the heterogeneous broadening of the final amorphous IrO_x structure. (**B**) Simulated O K-edge of rutile, anatase, brookite, and amorphous IrO_2, demonstrating the high degree of structural disorders in the Sr-doped amorphous IrO_x layer. Despite having well-defined local octahedral environment, the structural heterogeneity broadens the O 1s to O 2p–Ir 5d excitation into one single distribution. The simulated O K-edges were shifted to match the experimental O K-edge result at 4 hours. (**C**) Our proposed crystalline-to-amorphous transformation pathway in $SrIrO_3$. The oxygen loss from the lattice oxygen activation serves as the "seed" for the structural transformation. This activation step turns crystalline $SrIrO_3$ to Sr-doped amorphous IrO_x with a suggested square-planar motif. This square-planar structure has loose network, which allows Sr to dissolve further. After more Sr has dissolved, the square-planar structure collapses into a disordered mixture of Ir(III)/Ir(IV).

that the amorphization of $SrIrO_3$ results primarily in this structure, which we propose is the active moiety of $Sr_yIrO_x/SrIrO_3$: A hollandite-like (or romanechite-like) structure with Sr^{2+} stationed in the cavity helps to stabilize Ir^{3+}. Sun *et al.* (*32*) have demonstrated high OER activity on K_xIrO_2 hollandite, and Willinger *et al.* (*33*) have proposed that amorphous iridates have hollandite-like structural motifs and stressed the importance of Ir^{3+} on the OER catalysis. Our analysis agrees with the hypotheses of these early works.

The difference between the O K-edge of $Sr_yIrO_x/SrIrO_3$ after 4 hours and conventional amorphous IrO_x provides insights into how $Sr_yIrO_x/SrIrO_3$ is different from conventional amorphous IrO_x structure. In thermally or chemically grown amorphous IrO_x, the t_{2g} and e_g peaks are observable at the O K-edge (*26*), similar to crystalline rutile. In contrast, the O K-edge of $Sr_yIrO_x/SrIrO_3$ has a broad feature, indicating a more diverse oxygen environment—a sign of a greater extent of disorder. This greater extent of the disorder, in combination with the presence of romanechite/hollandite moieties, differentiates $Sr_yIrO_x/SrIrO_3$ from conventional amorphous IrO_x, which is more ordered based on their sharp t_{2g} and e_g features. From the comparison between TEY (probing the amorphous layer) and TFY (probing the whole $SrIrO_3$ film, both amorphous and crystalline parts) O K-edge NEXAFS (figs. S8 and S9), this unique structure is specific to the top Sr_yIrO_x layer and does not exist in bulk Sr-deficient $SrIrO_3$, although it has lost more than 40% of Sr. Increased proportion of defects generated from the destabilization of the active site/structure and the octahedral distortion has been suggested by several authors as means of increasing activity (*28*, *29*, *34*). We hypothesize that the unique structure of $SrIrO_3$ originates from its topochemical transformation, where the lattice oxygen activation initiates a coupled diffusion and structural transformation that creates a highly disordered iridate network. While we cannot unambiguously deconvolute how this final structure affects the electrocatalysis (e.g., structural, chemical, or electronic), the high extent of disorder of the amorphous IrO_x on $SrIrO_3$ differentiates it from other amorphous IrO_x structures. Our finding suggests that a synthesis that produces a highly disordered network, for example, via nonequilibrium approaches, for example, controlled diffusions or precipitations (*35*), could present an interesting avenue to develop comparatively active OER electrocatalysts. Additional studies are required to understand the influence of the electrochemical conditions (e.g., electrolyte components and operation potential windows) on the crystalline-to-amorphization transformations, in particular, in the middle of

the OER potential (*36*) and how these molecular transformations affect long-term stability.

In conclusion, we report the atomic details behind the crystalline-to-amorphous transformation of $SrIrO_3$ as a model system for the OER electrocatalysts. The surface structural transformation is triggered by the lattice oxygen activation. This step increases the oxygen vacancy concentration to destabilize the $SrIrO_3$ structure. This initial process transforms $SrIrO_3$ into amorphous Sr_yIrO_x with predominantly Ir square-planar motifs. The amorphous oxide then undergoes a second-stage transformation as more Sr^{2+} leaves the oxide. This final transformation creates a highly disordered structure containing Ir^{4+} octahedra with some remaining Sr^{2+}, which are likely accommodated in the cavities within the open romanechite- or hollandite-like structures. Our work explains how the active Sr_yIrO_x layer forms on $SrIrO_3$ and points to the critical role of the lattice oxygen activation and coupled ionic diffusion on the formation of the active OER units. In the case of $SrIrO_3$, the coupled Sr^{2+} and O^{2-} diffusion allow the structure to evolve into the final Sr_yIrO_x form that is more disordered than the electrochemically or thermally grown amorphous IrO_x. Our work provides insight into how applied potential facilitates the formation of the functional amorphous layers at the electrochemical interface and demonstrates how coupled ion diffusions activate the crystalline-to-amorphous transformation to form a highly disordered, amorphous oxide with high OER activity.

MATERIALS AND METHODS

MBE growth of $SrIrO_3$ thin films

The $SrIrO_3$ films were grown by MBE on single-crystal $DyScO_3$ (110) substrates (CrysTec GmbH) using a distilled ozone (O_3) oxidant at a background pressure of 10^{-6} torr and a growth temperature of 700°C. In bulk, both $SrIrO_3$ and $DyScO_3$ are orthorhombic, but they are only slightly distorted compared to cubic perovskite. The (110) orientation of $DyScO_3$ provides a surface facet similar to the (001) plane in the pseudo-cubic (pc) system. The resulting $(001)_{pc}$ $SrIrO_3$ film grown on $DyScO_3$ is under 0.05% biaxial compression at room temperature. Detailed growth parameters can be found in a previous publication (*25*).

Electrochemical characterization

Electrical contacts were made using the same protocol as reported previously (*21*). The nonreactive parts of the oxide were sealed using a chemically inert sample holder (made of Kel-F, polychlorotrifluoroethylene) to ensure that only the active surface was exposed to the electrolyte. All electrochemical characterization was conducted in a compact three-electrode cell (containing <10 ml of electrolyte volume) designed for rapid transfer to x-ray stations. We used a Biologic potentiostat. The reference was a Ag/AgCl redox couple in a saturated KCl solution, and the counter electrode was a Pt wire. The experiment was performed without an ohmic compensation; thus, the data presented in fig. S1 contain a resistance artifact that results in a relatively high Tafel slope (>300 mV/decade). All electrochemical measurements were performed in an Ar-saturated 0.1 M $HClO_4$ (99.999% trace metals basis, Sigma-Aldrich). All synchrotron x-ray characterizations were conducted within 1 hour from the electrochemical experiment, with the exception of XPS, which was done within 48 hours.

Synchrotron x-ray scattering

Synchrotron x-ray scattering of the $SrIrO_3$ films was conducted at undulator beamlines, 12ID-D and 33-ID-D, at the Advanced Photon Source (APS) on a six-circle Huber goniometer with an x-ray energy of 20 keV using a pixel array area detector (Dectris Pilatus 100K). The incoming x-ray beam had a flux of 10^{12} photons per second. The Q_z scans (L scans) were obtained after removing background contributions in the two-dimensional images. Our ex situ synchrotron-based surface x-ray scattering experiments of thin-film samples in the He environment excluded any beam damage effects on the amorphization of $SrIrO_3$.

Synchrotron XAS

The Sr L_{III}-edge, Ir M_{III}-edge, and O K-edge XAS detected in either TEY and TFY modes were carried out at the 4-ID-C beamline of the APS. The x-ray energy was calibrated using a reference measured simultaneously with the samples. Sr L_{III}-edge, Ir M_{III}-edge, and O K-edge XAS spectra normalization was performed by setting the intensity of the baseline before the absorption edge as zero. The Ir L_{III}-edge XANES and EXAFS measurements were conducted at beamline 20-ID-B of the APS in grazing incidence geometry and fluorescence mode after different cycling times with a polarization-dependent measurement (out-of-plane polarization). In the grazing incidence XAS measurement, the samples were aligned using x-ray, with controlled incidence angles. In this experimental configuration, the x-ray penetration thickness is directly related to the photon energy. The estimated penetration depth at the Ir L_{III}-edge x-ray energy is ~2.2 nm based on the calculation of the attenuation length using the $SrIrO_3$ mass density and the angle of incidence (https://henke.lbl.gov/optical_constants), which has an error bar of 0.1 nm. Bulk-sensitive Ir L_{III}-edge XANES of the pristine and cycled $SrIrO_3$ (SIO) films were also detected in fluorescence mode with an incidence angle of 45° at beamline 5-BM-D of the APS. The XANES data of references IrO_2 and $IrCl_3$ were collected at beamlines 20-ID-B and 5-BM-D in transmission mode. Ir L_{III}-edge XAS spectra including XANES and EXAFS were processed and analyzed using the Athena and Artemis programs (https://bruceravel.github.io/demeter).

Transmission electron microscopy

The TEM experiment was carried out using an FEI Titan microscope operated at 200 kV, which is equipped with an image corrector to correct both spherical and chromatic aberrations. The TEM specimen was prepared by mechanically grinding the substrate side down to about 100 μm thick, followed by cleaving the thinned sample into small pieces. Small pieces with sharp tips were chosen to glue on a copper oval grid with silver epoxy. These small pieces were oriented edge-on such that TEM specimen was along the cross-sectional view with respect to electron beam. This TEM specimen preparation method avoids any TEM specimen preparation artifacts such as ion beam damage and yields thin areas suitable for cross-sectional high-resolution TEM observations. Because of the arbitrary cleaving directions, different pieces may have different crystallographic orientations. As shown in Fig. 1D, the zone axis of the pristine and cycled pieces of $SrIrO_3/DyScO_3$ thin-film samples shows different crystallographic orientations.

X-ray photoelectron spectroscopy

XPS measurements were conducted using a PHI 5600 system with a base pressure of 1×10^{-10} torr. Monochromatized Al K_α radiation

($h\nu$ = 1486.7 eV), an electron analyzer pass energy of 23.5 eV, a 90° source-to-analyzer angle, and a 45° emission angle with respect to the sample surface were used for the experiments. The x-ray spot size was 1.5 × 3 mm^2, and the analysis area was 0.8 × 2 mm^2 (±7° solid angle). The XPS data were charge-corrected to the C 1s aliphatic carbon binding energy at 284.8 eV. A Shirley linear background was applied to all spectra to determine the total areas for the Ir 4f, Sr 3d, and O 1s transitions. Atomic percent values were calculated using the published sensitivity factors for the Perkin-Elmer PHI 5600 XPS system. The sensitivity factors for O 1s, Ir 4f, and Sr 3d are 0.711, 4.217, and 1.578, respectively. Ir 4f spectra were fit to two separate doublet peaks. Previous studies on IrO_2 thin films have shown both screened and unscreened final states, which is what likely accounts for the two separate doublets required to fit the Ir spectra. The screened component of the Ir oxide peak had binding energies of 62.3 ± 0.2 eV for Ir $4f_{7/2}$ and 65.3 ± 0.2 eV for Ir $4f_{5/2}$, while the unscreened component of the Ir oxide peak had binding energies of 63.6 ± 0.2 eV for Ir $4f_{7/2}$ and 66.6 ± 0.2 eV for Ir $4f_{5/2}$. All Ir 4f peaks were constrained to maintain a 4:3 ratio between the 7/2 and 5/2 peak intensities. Sr 3d spectra were additionally fit to two doublet peaks. The Sr $3d_{5/2}$ and Sr $3d_{3/2}$ peak were found to be 131.9 ± 0.1 and 133.7 ± 0.1 eV, respectively, for the first doublet. The second doublet represents another Sr compound, where the Sr $3d_{5/2}$ is found at 132.9 ± 0.2 eV and Sr $3d_{3/2}$ at 134.7 ± 0.2 eV for pristine $SrIrO_3$ and $SrIrO_3$ after 0.25 and 4 hours of cycling. All Sr 3d peaks were constrained to maintain a 3:2 ratio between the 5/2 and 3/2 peak intensities. The peak fits and positions agree well with previous literature (*21*). The electron attenuation lengths for each core level were calculated using the method of Cumpson and Seah (*37*), and the sampling depths were estimated considering a depth that contains 95% of the detected signal (*38*). Using this calculation, this results in sampling depths of 3.7, 3.6, and 2.7 nm for the Ir 4f, Sr 3d, and O 1s core levels, respectively.

DFT calculations

All energy computations were performed using VASP (Vienna Ab initio Simulation Package) with a *k*-point sampling of 1000 per atoms (*39*). The inputs were generated using pymatgen (*40*). The plane-wave energy cutoff was set to 400 eV. The exchange correlation functional used was Generalized Gradient Approximation-Revised Perdew-Burke-Ernzerhof (GGA-RPBE) unless specified otherwise. All structures were relaxed to reach forces lower than 0.01 eV/A. The ion energies have been extracted from experimental data using the approach of Persson *et al.* (*41*). The K-edge XANES spectra were computed using the FEFF9 code, which uses the Green's formulation of the multiple scattering theory to compute the spectra (*42*). The x-ray absorption μ is computed in a manner similar to Fermi's golden rule when written in terms of the projected photoelectron density of final states or the imaginary part of the one-particle Green's function. We used the set of optimized FEFF parameters, which were benchmarked in (*43*) and determined to achieve the best balance between the computational cost and convergence performance.

SUPPLEMENTARY MATERIALS

Supplementary material for this article is available at http://advances.sciencemag.org/cgi/content/full/7/2/eabc7323/DC1

REFERENCES AND NOTES

1. T. R. Cook, D. K. Dogutan, S. Y. Reece, Y. Surendranath, T. S. Teets, D. G. Nocera, Solar energy supply and storage for the legacy and non legacy worlds. *Chem. Rev.* **110**, 6474–6502 (2010).
2. M. G. Walter, E. L. Warren, J. R. McKone, S. W. Boettcher, Q. Mi, E. A. Santori, N. S. Lewis, Solar water splitting cells. *Chem. Rev.* **110**, 6446–6473 (2010).
3. J. W. Ager, A. A. Lapkin, Chemical storage of renewable energy. *Science* **360**, 707–708 (2018).
4. Z. W. Seh, J. Kibsgaard, C. F. Dickens, I. Chorkendorff, J. K. Norskov, T. F. Jaramillo, Combining theory and experiment in electrocatalysis: Insights into materials design. *Science* **355**, eaad4998 (2017).
5. V. R. Stamenkovic, D. Strmcnik, P. P. Lopes, N. M. Markovic, Energy and fuels from electrochemical interfaces. *Nat. Mater.* **16**, 57–69 (2017).
6. S. Geiger, O. Kasian, M. Ledendecker, E. Pizzutilo, A. M. Mingers, W. T. Fu, O. Diaz-Morales, Z. Li, T. Oellers, L. Fruchter, A. Ludwig, K. J. J. Mayrhofer, M. T. M. Koper, S. Cherevko, The stability number as a metric for electrocatalyst stability benchmarking. *Nat. Catal.* **1**, 508–515 (2018).
7. E. Fabbri, M. Nachtegaal, T. Binninger, X. Cheng, B.-J. Kim, J. Durst, F. Bozza, T. Graule, R. Schäublin, L. Wiles, M. Pertoso, N. Danilovic, K. E. Ayers, T. J. Schmidt, Dynamic surface self-reconstruction is the key of highly active perovskite nano-electrocatalysts for water splitting. *Nat. Mater.* **16**, 925–931 (2017).
8. K. J. May, C. E. Carlton, K. A. Stoerzinger, M. Risch, J. Suntivich, Y.-L. Lee, A. Grimaud, Y. Shao-Horn, Influence of oxygen evolution during water oxidation on the surface of perovskite oxide catalysts. *J. Phys. Chem. Lett.* **3**, 3264–3270 (2012).
9. S. Samira, X.-K. Gu, E. Nikolla, Design strategies for efficient nonstoichiometric mixed metal oxide electrocatalysts: Correlating measurable oxide properties to electrocatalytic performance. *ACS Catal.* **9**, 10575–10586 (2019).
10. J. T. Mefford, X. Rong, A. M. Abakumov, W. G. Hardin, S. Dai, A. M. Kolpak, K. P. Johnston, K. J. Stevenson, Water electrolysis on $La_{1-x}Sr_xCoO_{3-\delta}$ perovskite electrocatalysts. *Nat. Commun.* **7**, 11053 (2016).
11. T. Binninger, R. Mohamed, K. Waltar, E. Fabbri, P. Levecque, R. Kötz, T. J. Schmidt, Thermodynamic explanation of the universal correlation between oxygen evolution activity and corrosion of oxide catalysts. *Sci. Rep.* **5**, 12167 (2015).
12. A. Grimaud, O. Diaz-Morales, B. Han, W. T. Hong, Y.-L. Lee, L. Giordano, K. A. Stoerzinger, M. T. M. Koper, Y. Shao-Horn, Activating lattice oxygen redox reactions in metal oxides to catalyse oxygen evolution. *Nat. Chem.* **9**, 457–465 (2017).
13. A. Bergmann, E. Martinez-Moreno, D. Teschner, P. Chernev, M. Gliech, J. F. de Araújo, T. Reier, H. Dau, P. Strasser, Reversible amorphization and the catalytically active state of crystalline Co_3O_4 during oxygen evolution. *Nat. Commun.* **6**, 8625 (2015).
14. A. Indra, P. W. Menezes, N. R. Sahraie, A. Bergmann, C. Das, M. Tallarida, D. Schmeißer, P. Strasser, M. Driess, Unification of catalytic water oxidation and oxygen reduction reactions: Amorphous beat crystalline cobalt iron oxides. *J. Am. Chem. Soc.* **136**, 17530–17536 (2014).
15. G. Chen, W. Zhou, D. Guan, J. Sunarso, Y. Zhu, X. Hu, W. Zhang, Z. Shao, Two orders of magnitude enhancement in oxygen evolution reactivity on amorphous $Ba_{0.5}Sr_{0.5}Co_{0.8}Fe_{0.2}O_{3-\delta}$ nanofilms with tunable oxidation state. *Sci. Adv.* **3**, e1603206 (2017).
16. A. Grimaud, A. Demortière, M. Saubanère, W. Dachraoui, M. Duchamp, M.-L. Doublet, J.-M. Tarascon, Activation of surface oxygen sites on an iridium-based model catalyst for the oxygen evolution reaction. *Nat. Energy* **2**, 16189 (2017).
17. O. Diaz-Morales, S. Raaijman, R. Kortlever, P. J. Kooyman, T. Wezendonk, J. Gascon, W. T. Fu, M. T. M. Koper, Iridium-based double perovskites for efficient water oxidation in acid media. *Nat. Commun.* **7**, 12363 (2016).
18. N. Danilovic, R. Subbaraman, K.-C. Chang, S. H. Chang, Y. J. Kang, J. Snyder, A. P. Paulikas, D. Strmcnik, Y.-T. Kim, D. Myers, V. R. Stamenkovic, N. M. Markovic, Activity-stability trends for the oxygen evolution reaction on monometallic oxides in acidic environments. *J. Phys. Chem. Lett.* **5**, 2474–2478 (2014).
19. O. Kasian, S. Geiger, T. Li, J.-P. Grote, K. Schweinar, S. Zhang, C. Scheu, D. Raabe, S. Cherevko, B. Gault, K. J. J. Mayrhofer, Degradation of iridium oxides *via* oxygen evolution from the lattice: Correlating atomic scale structure with reaction mechanisms. *Energ. Environ. Sci.* **12**, 3548–3555 (2019).
20. G. C. da Silva, N. Perini, E. A. Ticianelli, Effect of temperature on the activities and stabilities of hydrothermally prepared IrO_x nanocatalyst layers for the oxygen evolution reaction. *Appl. Catal. B-Environ.* **218**, 287–297 (2017).
21. L. C. Seitz, C. F. Dickens, K. Nishio, Y. Hikita, J. Montoya, A. Doyle, C. Kirk, A. Vojvodic, H. Y. Hwang, J. K. Norskov, T. F. Jaramillo, A highly active and stable $IrO_x/SrIrO_3$ catalyst for the oxygen evolution reaction. *Science* **353**, 1011–1014 (2016).
22. R. H. Zhang, N. Dubouis, M. B. Osman, W. Yin, M. T. Sougrati, D. A. D. Corte, D. Giaume, A. Grimaud, A dissolution/precipitation equilibrium on the surface of iridium-based perovskites controls their activity as oxygen evolution reaction catalysts in acidic media. *Angew. Chem. Int. Ed.* **58**, 4571–4575 (2019).
23. A. R. Akbashev, L. Zhang, J. T. Mefford, J. Park, B. Butz, H. Luftman, W. C. Chueh, A. Vojvodic, Activation of ultrathin $SrTiO_3$ with subsurface $SrRuO_3$ for the oxygen evolution reaction. *Energ. Environ. Sci.* **11**, 1762–1769 (2018).

24. R. Tang, Y. Nie, J. K. Kawasaki, D.-Y. Kuo, G. Petretto, G. Hautier, G.-M. Rignanese, K. M. Shen, D. G. Schlom, J. Suntivich, Oxygen evolution reaction electrocatalysis on $SrIrO_3$ grown using molecular beam epitaxy. *J. Mater. Chem. A* **4**, 6831–6836 (2016).
25. Y. F. Nie, P. D. C. King, C. H. Kim, M. Uchida, H. I. Wei, B. D. Faeth, J. P. Ruf, J. P. C. Ruff, L. Xie, X. Pan, C. J. Fennie, D. G. Schlom, K. M. Shen, Interplay of spin-orbit interactions, dimensionality, and octahedral rotations in semimetallic $SrIrO_3$. *Phys. Rev. Lett.* **114**, 016401 (2015).
26. T. Reier, Z. Pawolek, S. Cherevko, M. Bruns, T. Jones, D. Teschner, S. Selve, A. Bergmann, H. N. Nong, R. Schlögl, K. J. J. Mayrhofer, P. Strasser, Molecular insight in structure and activity of highly efficient, Low-Ir Ir-Ni oxide catalysts for electrochemical water splitting (OER). *J. Am. Chem. Soc.* **137**, 13031–13040 (2015).
27. J. J. Zhang, A. S. Botana, J. W. Freeland, D. Phelan, H. Zheng, V. Pardo, M. R. Norman, J. F. Mitchell, Large orbital polarization in a metallic square-planar nickelate. *Nat. Phys.* **13**, 864–869 (2017).
28. V. Pfeifer, T. E. Jones, J. J. V. Vélez, C. Massué, M. T. Greiner, R. Arrigo, D. Teschner, F. Girgsdies, M. Scherzer, J. Allan, M. Hashagen, G. Weinberg, S. Piccinin, M. Hävecker, A. Knop-Gericke, R. Schlögl, The electronic structure of iridium oxide electrodes active in water splitting. *Phys. Chem. Chem. Phys.* **18**, 2292–2296 (2016).
29. V. Pfeifer, T. E. Jones, S. Wrabetz, C. Massué, J. J. Velasco Vélez, R. Arrigo, M. Scherzer, S. Piccinin, M. Hävecker, A. Knop-Gericke, R. Schlögl, Reactive oxygen species in iridium-based OER catalysts. *Chem. Sci.* **7**, 6791–6795 (2016).
30. B. Prasai, B. Cai, M. K. Underwood, J. P. Lewis, D. A. Drabold, Properties of amorphous and crystalline titanium dioxide from first principles. *J. Mater. Sci.* **47**, 7515–7521 (2012).
31. S. K. Gautam, A. Das, S. Ojha, D. K. Shukla, D. M. Phase, F. Singh, Electronic structure modification and Fermi level shifting in niobium-doped anatase titanium dioxide thin films: A comparative study of NEXAFS, work function and stiffening of phonons. *Phys. Chem. Chem. Phys.* **18**, 3618–3627 (2016).
32. W. Sun, Y. Song, X.-Q. Gong, L.-M. Cao, J. Yang, Hollandite structure $K_{x\approx0.25}IrO_2$ catalyst with highly efficient oxygen evolution reaction. *ACS Appl. Mater. Interfaces* **8**, 820–826 (2016).
33. E. Willinger, C. Massué, R. Schlögl, M. G. Willinger, Identifying key structural features of IrO_x water splitting catalysts. *J. Am. Chem. Soc.* **139**, 12093–12101 (2017).
34. Z. Xu, J. R. Kitchin, Tuning oxide activity through modification of the crystal and electronic structure: From strain to potential polymorphs. *Phys. Chem. Chem. Phys.* **17**, 28943–28949 (2015).
35. R. D. L. Smith, M. S. Prévot, R. D. Fagan, Z. Zhang, P. A. Sedach, M. K. J. Siu, S. Trudel, C. P. Berlinguette, Photochemical route for accessing amorphous metal oxide materials for water oxidation catalysis. *Science* **340**, 60–63 (2013).
36. H. G. S. Casalongue, M. L. Ng, S. Kaya, D. Friebel, H. Ogasawara, A. Nilsson, In situ observation of surface species on iridium oxide nanoparticles during the oxygen evolution reaction. *Angew. Chem. Int. Ed.* **53**, 7169–7172 (2014).
37. P. J. Cumpson, M. P. Seah, Elastic scattering corrections in AES and XPS. II. Estimating attenuation lengths and conditions required for their valid use in overlayer/substrate experiments. *Surf. Interface Anal.* **25**, 430–446 (1997).
38. C. J. Powell, Practical guide for inelastic mean free paths, effective attenuation lengths, mean escape depths, and information depths in x-ray photoelectron spectroscopy. *J. Vac. Sci. Technol. A* **38**, 023209 (2020).
39. G. Kresse, J. Furthmuller, Efficiency of ab-initio total energy calculations for metals and semiconductors using a plane-wave basis set. *Comput. Mater. Sci.* **6**, 15–50 (1996).
40. S. P. Ong, W. D. Richards, A. Jain, G. Hautier, M. Kocher, S. Cholia, D. Gunter, V. L. Chevrier, K. A. Persson, G. Ceder, Python materials genomics (pymatgen): A robust, open-source python library for materials analysis. *Comput. Mater. Sci.* **68**, 314–319 (2013).
41. K. A. Persson, B. Waldwick, P. Lazic, G. Ceder, Prediction of solid-aqueous equilibria: Scheme to combine first-principles calculations of solids with experimental aqueous states. *Phys. Rev. B* **85**, 235438 (2012).
42. J. J. Rehr, J. J. Kas, M. P. Prange, A. P. Sorini, Y. Takimoto, F. Vila, *Ab initio* theory and calculations of x-ray spectra. *C. R. Phys.* **10**, 548–559 (2009).
43. K. Mathew, C. Zheng, D. Winston, C. Chen, A. Dozier, J. J. Rehr, S. P. Ong, K. A. Persson, High-throughput computational x-ray absorption spectroscopy. *Sci. Data* **5**, 180151 (2018).

Acknowledgments

Funding: This work was supported by the U.S. Department of Energy (DOE), Office of Science, Basic Energy Sciences under award DE-SC0018029. D.D.F. was supported by the U.S. Department of Energy, Office of Science, Office of Basic Energy Sciences, Materials Sciences and Engineering Division. This research used resources of the Advanced Photon Source and Center for Nanoscale Materials, U.S. DOE Office of Science User Facilities operated for the DOE Office of Science by Argonne National Laboratory under contract no. DE-AC02-06CH11357, and the Canadian Light Source and its funding partners. Part of this research was conducted at the Northwest Nanotechnology Infrastructure, a National Nanotechnology Coordinated Infrastructure (NNCI) site at Oregon State University, which is supported, in part, by the NSF (grant NNCI-1542101) and Oregon State University. J.N.N. acknowledges support from the NSF Graduate Research Fellowship under grant no. DGE-1650441. This work made use of the Cornell Center for Materials Research Shared Facilities, which are supported through the NSF MRSEC program (DMR-1719875). Substrate preparation was performed, in part, at the Cornell NanoScale Facility, a member of the NNCI, which is supported by the NSF (grant no. ECCS-1542081). The computational part of this work was supported by the Fonds de la Recherche Scientifique-FNRS under grant no. 29120589. We acknowledge access to various computational resources: the Tier-1 supercomputer of the Fédération Wallonie-Bruxelles funded by the Walloon Region (grant agreement no. 1117545) and all the facilities provided by the Université Catholique de Louvain (CISM/UCL) and by the Consortium des Équipements de Calcul Intensif en Fédération Wallonie-Bruxelles (CECI). J. Suntivich acknowledges support from the Sloan Research Fellowship. J.N.N., K.M.S., and D.G.S. acknowledge support from the NSF under Cooperative Agreement DMR-1539918 [Platform for the Accelerated Realization, Analysis, and Discovery of Interface Materials (PARADIM)] and DMR-1709255 (Condensed Matter Physics) for sample growth. **Author contributions:** J. Suntivich, H.Z., and Z.F. initiated the collaboration and conceived the work. H.Z. and G.W. designed the experiments. J.N.N. prepared the $SrIrO_3$ films with advice from K.M.S. and D.G.S. G.W., H.Z., and Y.D. conducted the x-ray scattering experiments and analyses. G.W., H.Z., R.K., and C.-J.S. conducted the GI-XAS measurements and analyses. J.W., G.W., J. Sun, and S.C. conducted the TEM experiments and analyses. G.W. conducted the electrochemical experiments. G.W. and J.W.F. conducted the soft XAS experiments. J. Suntivich, H.Z., D.D.F., G.W., G.H., J.K., D.-Y.K., and J.W.F. analyzed the interpretation and provided mechanistic discussions. J.T.D. and G.S.H. conducted the XPS measurement. J.K., G.P., G.-M.R., and G.H. conducted the theoretical calculations and analyses. G.W., D.D.F., J.W.F., G.S.H., Z.F., H.Z., and J. Suntivich drafted and revised the manuscript. All authors agree on the contents and conclusion of the paper. **Competing interests:** The authors declare that they have no competing interests. **Data and materials availability:** All data needed to evaluate the conclusions in the paper are present in the paper and/or the Supplementary Materials. Additional data related to this paper may be requested from the authors.

Submitted 11 May 2020
Accepted 18 November 2020
Published 8 January 2021
10.1126/sciadv.abc7323

Citation: G. Wan, J. W. Freeland, J. Kloppenburg, G. Petretto, J. N. Nelson, D.-Y. Kuo, C.-J. Sun, J. Wen, J. T. Diulus, G. S. Herman, Y. Dong, R. Kou, J. Sun, S. Chen, K. M. Shen, D. G. Schlom, G.-M. Rignanese, G. Hautier, D. D. Fong, Z. Feng, H. Zhou, J. Suntivich, Amorphization mechanism of $SrIrO_3$ electrocatalyst: How oxygen redox initiates ionic diffusion and structural reorganization. *Sci. Adv.* **7**, eabc7323 (2021).

Amorphization mechanism of $SrIrO_3$ electrocatalyst: How oxygen redox initiates ionic diffusion and structural reorganization

Gang Wan, John W. Freeland, Jan Kloppenburg, Guido Petretto, Jocienne N. Nelson, Ding-Yuan Kuo, Cheng-Jun Sun, Jianguo Wen, J. Trey Diulus, Gregory S. Herman, Yongqi Dong, Ronghui Kou, Jingying Sun, Shuo Chen, Kyle M. Shen, Darrell G. Schlom, Gian-Marco Rignanese, Geoffroy Hautier, Dillon D. Fong, Zhenxing Feng, Hua Zhou and Jin Suntivich

Sci Adv **7** (2), eabc7323.
DOI: 10.1126/sciadv.abc7323